Intensity and Phase Statistics of Multilook Polarimetric and Interferometric SAR Imagery

Jong-Sen Lee, *Senior Member, IEEE,* Karl W. Hoppel, Stephen A. Mango, *Member, IEEE,* and Allen R. Miller

Abstract—**Polarimetric and interferometric SAR data are frequently multilook processed for speckle reduction and data compression. The statistical characteristics of multilook data are quite different from those of single-look data. In this paper, we investigate the statistics of their intensity and phase. Probability density function (PDF's) of the multilook phase difference, magnitude of complex product, and intensity and amplitude ratios between two components of the scattering matrix are derived, and expressed in closed forms. The PDF's depend on the complex correlation coefficient and the number of looks. Comparisons of these theoretically derived PDF's are made to measurements from NASA/JPL AIRSAR data. The results of this paper can be applied to feature classification using polarimetric SAR and to the estimation of decorrelation effects of the interferometric SAR.**

I. Introduction

RECENT advances in polarimetric and interferometric radar technology have stimulated research toward understanding scattering mechanisms and toward the reliable classification of targets and terrain covers. The polarimetric radar provides a large amount of scattering information embedded in a Mueller matrix, or equivalently, in a polarimetric covariance matrix. The intensity and amplitude statistics of SAR images, such as *L*-band and *HH* for SEASAT and SIR-B, and *C*-band *VV* for ERS-1, have been extensively investigated for various terrain, ground cover, and ocean surfaces. Less well known are the statistics between multiple channels of polarimetric or interferometric SAR's, especially for the multilook processed data. Most mathematical modeling and verification efforts (see [1] and [2]) were aiming at the single-look processed data. However, for speckle reduction and data compression, polarimetric and interferometric radar data are frequently multilook processed. For example, the NASA/JPL AIRSAR data are obtained by averaging the Mueller matrices of many single-look pixels in the azimuth direction to achieve effective 4-look or 16-look processing.

The statistical characteristics of multilook data depart considerably from those of single-look data. In this paper, an analytical method is introduced to compute various statistics of multilook polarimetric and interferometric SAR data based on the circular Gaussian assumption. The polarimetric covariance matrix is found having a complex Wishart distribution [3]. Based on this distribution, probability density functions (PDF's) of the multilook phase difference, amplitude and intensity ratios between copolarized and cross-polarized terms, and the magnitude and phase of interferogrametric measurements [4] are derived. Lopes *et al.* [17] previously derived the phase difference PDF's in a more complicated form. In this paper, closed-form solutions are found by multiple integrations of special functions. Various statistics, such as the mean and the standard deviation for each PDF are computed as a function of the correlation coefficient and the number of looks.

The PDF's derived in this paper can be used to derive maximum likelihood distance measures for feature classification. The 1-look cases have been investigated by Lim *et al.* [18], and the multilook cases using the complete polarimetric covariance matrix have been investigated by Lee et al. [19]. The distance measures for the multilook phase difference, magnitude of product, and amplitude ratio can be used for the situations in which either complete polarimetric measurements are not available, or it is preferred to use data from selected frequencies and polarizations. For interferometric SAR, the statistics of interferograms derived in this paper can be applied to the estimation of decorrelation effects [4].

NASA/JPL 1-look and 4-look AIRSAR data of Howland Forest and San Francisco were used for comparison. Histograms from 1-look SAR data agreed with theoretical PDF's. However, discrepancies were found when matching the 4-look polarimetric data with the 4-look PDF's. Instead, we found that the 3-look PDF's matched better. The problem was traced to the averaging of correlated 1-look pixels. We also compared these theoretical PDF's for forest, ocean surfaces, park areas, and city blocks. We found that the agreement between histograms and theoretical PDF's are good for the phase difference and the amplitude ratio. However, discrepancies exist in the agreement for the magnitude of product. The merits of this complex Gaussian model are discussed.

II. Multilook Polarimetric Radar Data and the Complex Wishart Distribution

A polarimetric radar [11] measures the complete scattering matrix S of a medium at a given incidence angle:

$$S = \begin{bmatrix} S_{hh} & S_{hv} \\ S_{vh} & S_{vv} \end{bmatrix}. \quad (1)$$

Manusript received October 29, 1993; revised March 28, 1994.

J.-S. Lee, K. W. Hoppel, and S. A. Mango are with the Remote Sensing Division, Code 7230, Naval Research Laboratory, Washington, DC 20375.

A. R. Miller is with the Department of Mathematics, George Washington University, Washington, DC 20052.

IEEE Log Number 9403645.

Theoretically, the copolarized components (i.e., *HH* and *VV*) are correlated, while the correlation between copolarized and cross-polarized terms, for example, *HV* and *HH*, is zero. However, evidence from polarimetric SAR data has indicated that the latter may also be correlated but at a lower level. This is probably due to channel crosstalk, thermal noise, and the inaccuracy of theoretical modeling.

For a reciprocal medium, the three unique elements define a complex vector:

$$\boldsymbol{u} = \begin{bmatrix} S_1 \\ S_2 \\ S_3 \end{bmatrix} \tag{2}$$

where for convenience we have used S_1, S_2, and S_3 to denote S_{hh}, S_{vv}, and S_{hv} in any order. For nonreciprocal medium or for bistatic radars, the dimension of vector $\boldsymbol{u}$ is 4. When the radar illuminates an area of a random surface containing many elementary scatterers, $\boldsymbol{u}$ can be modeled as having a multivariate complex Gaussian distribution (Goodman [3]):

$$p_u(\boldsymbol{u}) = \frac{1}{\pi^3 |C|} \exp\left(-\boldsymbol{u}^T C^{-1} \boldsymbol{u}\right) \tag{3}$$

where the complex covariance matrix, $C = E[\boldsymbol{u}\boldsymbol{u}^T]$, the superscript T denotes complex conjugate transpose, and $|C|$ is the determinant of C. The complex covariance matrix is Hermitian, i.e., $C = C^T$. The real and imaginary parts of any two complex elements of $\boldsymbol{u}$ are assumed to have circular Gaussian distribution [5]. For $S_j = x_j + iy$, the circular Gaussian assumption requires that x_j and y_j for $j = 1, 2, 3$ have joint Gaussian distribution and satisfy the following conditions: $E[x_j] = E[y_j] = 0$, $E[x_j^2] = E[y_j^2]$, $E[x_j y_j] = 0$, $E[x_j x_k] = E[y_j y_k]$, and $E[y_j x_k] = -E[x_j y_k]$. The circular Gaussian assumption has been shown to be valid for polarimetric SAR data [2].

Polarimetric SAR data can also be represented by a Mueller matrix. The Mueller matrix M is a real 4×4 symmetrical matrix, and the elements of the Mueller matrix are related to the polarimetric covariance matrix, $\boldsymbol{u}\boldsymbol{u}^T$. SAR data are frequently multilook processed for speckle reduction and data compression. The NASA/JPL aircraft SAR processor compresses polarimetric data by averaging Mueller matrices of four 1-look pixels in the azimuth direction to form 4-look Mueller matrix SAR images. JPL's new frame processor [6] produces 16-look polarimetric SAR imagery. Since the elements of the Mueller matrix are linear combinations of elements of the covariance matrix, conversion from the averaged Mueller matrix to the covariance matrix produces results identical to averaging covariance matrices.

Multilook polarimetric SAR processing requires averaging several independent 1-look covariance matrices. The n-look covariance matrix is

$$Z = \frac{1}{\boldsymbol{n}} \sum_{k=1}^{n} \boldsymbol{u}(k)\boldsymbol{u}(k)^T \tag{4}$$

where $\boldsymbol{n}$ is the number of looks, and the vector $\boldsymbol{u}(k)$ is the kth 1-look sample. Let $A = nZ$. The matrix A has a complex Wishart distribution (Goodman [3]):

$$p_A^{(n)}(A) = \frac{|A|^{n-q} \exp\left[-\mathrm{Tr}\,(C^{-1}A)\right]}{K(\boldsymbol{n}, q)|C|^n}. \tag{5}$$

where $\mathrm{Tr}\,(C^{-1}A)$ denotes the trace of $C^{-1}A$, and

$$K(\boldsymbol{n}, q) = \pi^{(1/2)q(q-1)}\Gamma(n) \cdots \Gamma(\boldsymbol{n} - q + 1). \tag{6}$$

The parameter q is the dimension of vector $\boldsymbol{u}$, and $\Gamma(\,)$ is the Gamma function. For monostatic polarimetric SAR on a reciprocal medium, $q = 3$. The random variables of this distribution are $A_{11}, \cdots, A_{qq}, A_{12R}, A_{12I}, A_{(p-1)qR}$, $A_{(p-1)qI}$, where the subscripts R and I denote the real and imagery parts, respectively. The total number of independent variables is q^2. The distribution for the multilook covariance matrix Z, can be easily obtained using (5):

$$p_Z^{(n)}(Z) = \frac{\boldsymbol{n}^{qn}|Z|^{n-q} \exp\left[-\boldsymbol{n}\ \mathrm{Tr}\,(C^{-1}Z)\right]}{K(\boldsymbol{n}, q)|C|^n}. \tag{7}$$

The domain of A is limited by Z being positive definite.

For $q = 1$, we have the well-known one-dimensional multilook intensity distribution

$$p_{Z_{11}}^{(n)}(Z_{11}) = \frac{\boldsymbol{n}^n Z_{11}^{n-1} \exp\left[-\boldsymbol{n}Z_{11}/C_{11}\right]}{\Gamma(\boldsymbol{n})C_{11}^n} \tag{8}$$

where Z_{11} is the n-look intensity and $C_{11} = E[S_1 S_1^*] = E[Z_{11}]$.

Applying the complex Wishart distribution, Murza [16] derived a distribution for the Stokes vector, and Lopes *et al.* [17] related phase differences to forest parameters. In this paper, various PDF's of the phase difference, the magnitude of complex product, and the amplitude and intensity ratios, and so forth, of multilook returns are presented. They should be of interest to researchers in polarimetric radar data analysis. They should also contribute to the study of the phase error in the radar interferometry. These PDF's are derived using (5). It is slightly more complicated in notations, if (7) is used for the derivation.

III. The Correlation Coefficient of Multilook Radar Echoes

The complex correlation coefficient is the most important parameter in describing the PDF's. The complex correlation coefficient is defined as

$$\rho_c = \frac{E[S_i S_j^*]}{\sqrt{E[|S_i|^2]E[|S_j|^2]}} = |\rho_c| e^{i\theta} \tag{9}$$

where S_i and S_j are any two components of the scattering matrix or the two radar returns from polarimetric or interferometric SAR. For multilook polarimetric radar data represented by the Mueller matrix, ρ_c can be evaluated by averaging the Mueller matrix of neighboring pixels in a homogeneous area. The magnitude of ρ_c can also be estimated using two multilook intensities Z_{ii} and Z_{jj}. The correlation coefficient of the n-look intensities is defined

as

$$\rho_I^{(n)} = \frac{E[(Z_{ii} - \bar{Z}_{ii})(Z_{jj} - \bar{Z}_{jj})]}{\sqrt{E[(Z_{ii} - \bar{Z}_{ii})^2]E[Z_{jj} - \bar{Z}_{jj})^2]}} \tag{10}$$

and it is shown in Appendix A that

$$\rho_I^{(n)} = |\rho_c|^2. \tag{11}$$

Equation (11) shows that $\rho_I^{(n)}$ is independent of the number of looks n.

The analysis of correlations, using polarimetric AIRSAR data of San Francisco and Howland forest, indicated that *HH* and *VV* components over the ocean surface have high correlation near 0.9, and in forest areas, the correlation has a lower value around 0.5. The correlations in the city blocks and park areas are small with values of 0.3 and 0.25, respectively.

IV. Multilook Phase-Difference Distribution

The phase-difference PDF is derived in this section for any two components of polarimetric SAR. This phase difference is also the phase of the interferogram. The 1-look phase difference is defined as

$$\psi_1 = \text{Arg}\,(S_i S_j^*). \tag{12}$$

The multilook phase is obtained by

$$\psi_n = \text{Arg}\left[\frac{1}{\boldsymbol{n}} \sum_{k=1}^{n} S_i(k) S_j^*(k)\right]. \tag{13}$$

The ψ_n is the argument of a off-diagonal term in the covariance matrix Z. It should be noted that the average of 1-look phase differences to produce the multilook would be erroneous due to the 2π phase wrapping. For notational convenience, the subscript n of ψ_n will be omitted.

Since all the PDF's to be derived involve only two components, the distribution of A with $q = 2$ is used in the PDF derivation. For $q = 2$, we can write

$$A = \begin{bmatrix} A_{11} & \alpha e^{i\psi} \\ \alpha e^{-i\psi} & A_{22} \end{bmatrix} \tag{14}$$

and

$$C = \begin{bmatrix} C_{11} & \sqrt{C_{11}C_{22}}\,|\rho_c|\,e^{i\theta} \\ \sqrt{C_{11}C_{22}}\,|\rho_c|\,e^{-i\theta} & C_{22} \end{bmatrix} \tag{15}$$

where $A_{12R} + iA_{12I} = \alpha e^{i\psi}$, and $C_{ii} = E[|S_i|^2]$. For convenience, we normalize the intensities of A_{11} and A_{22}, and α by

$$B_1 = \frac{A_{11}}{C_{11}} \qquad B_2 = \frac{A_{22}}{C_{22}} \qquad \eta = \frac{\alpha}{\sqrt{C_{11}C_{22}}}. \tag{16}$$

By changing variables from A_{11}, A_{22}, A_{12R}, and A_{12I} to B_1, B_2, η and ψ, respectively, (5) becomes

$$p(B_1, B_2, \eta, \psi) = \frac{(B_1B_2 - \eta^2)^{n-2}\eta}{\pi(1 - |\rho_c|^2)^n \Gamma(\boldsymbol{n})\Gamma(\boldsymbol{n} - 1)} \exp\left(-\frac{B_1 + B_2 - 2\eta|\rho_c|\cos(\psi - \theta)}{(1 - |\rho_c|^2)}\right). \tag{17}$$

Equation (17) is not a function of C_{11} and C_{22}. The PDF of ψ is obtained by integrating (17) over B_1, B_2, and η. The integration domain is constrained by $B_1B_2 - \eta^2 > 0$. The derivation has been given by Lee *et al.* [7]. The multilook phase-difference distribution is

$$p_\psi^{(n)}(\psi) = \frac{\Gamma(n + 1/2)(1 - |\rho_c|^2)^n\beta}{2\sqrt{\pi}\Gamma(\boldsymbol{n})(1 - \beta^2)^{n+1/2}} + \frac{(1 - |\rho_c|^2)^n}{2\pi} \cdot F(\boldsymbol{n}, 1; 1/2; \beta^2), \qquad -\pi < \psi \le \pi \tag{18}$$

with

$$\beta = |\rho_c|\cos(\psi - \theta) \tag{19}$$

where $F(\boldsymbol{n}, 1; 1/2; \beta^2)$ is a Gauss hyperogeometric function. An alternative expression for the phase-difference distribution in higher order hypergeometric functions was independently derived by Lopes *et al.* [17].

The hypergeometric function can be replaced by trigonometric and algebraic functions for small $\boldsymbol{n}$. For example, the 1-look ($\boldsymbol{n} = 1$) PDF can be obtained by applying the following identity:

$$F(1, 1; 1/2; z) = (1 - z)^{-1}\left[1 + \frac{\sqrt{z}\sin^{-1}\sqrt{z}}{\sqrt{1 - z}}\right] \tag{20}$$

Using (18), results in the 1-look phase-difference PDF

$$p_\psi^{(1)}(\psi) = \frac{(1 - |\rho_c|^2)[(1 - \beta^2)^{1/2} + \beta(\pi - \cos^{-1}\beta)]}{2\pi(1 - \beta^2)^{3/2}}. \tag{21}$$

This 1-look phase-difference PDF is identical to the results obtained by Kong [1] and Sarabandi [2]. Similarly, for the convenience in applications, the 2-look, 3-look, and 4-look phase-difference PDF's can also be derived and expressed in algebraic and trigonmetric functions. The 2-look phase-difference PDF is

$$p_\psi^{(2)}(\psi) = \frac{3}{8}\frac{(1 - |\rho_c|^2)^2\beta}{(1 - \beta^2)^{5/2}} + \frac{(1 - |\rho_c|^2)^2}{4\pi(1 - \beta^2)^2} \cdot \left[2 + \beta^2 + \frac{3\beta}{(1 - \beta^2)^{1/2}}\sin^{-1}(\beta)\right]. \tag{22}$$

The 3-look phase-difference PDF is

$$p_\psi^{(3)}(\psi) = \frac{15}{32}\frac{(1 - |\rho_c|^2)^3\beta}{(1 - \beta^2)^{7/2}} + \frac{(1 - |\rho_c|^2)^3(1 - \beta^2)^{-3}}{16\pi} \cdot \left[8 + 9\beta^2 - 2\beta^4 + \frac{15\beta}{(1 - \beta^2)^{1/2}}\sin^{-1}(\beta)\right]. \tag{23}$$

The 4-look phase-difference PDF is

$$p_{\psi}^{(4)}(\psi) = \frac{35(1 - |\rho_c|^2)^4\beta}{64(1 - \beta^2)^{9/2}} + \frac{(1 - |\rho_c|^2)^4}{96\pi(1 - \beta^2)^4} \cdot \left[48 + 87\beta^2 - 38\beta^4 + 8\beta^6 + \frac{105\beta}{(1 - \beta^2)^{1/2}} \sin^{-1}(\beta)\right]. \quad (24)$$

The PDF of (18) depends only on the number of looks and the complex correlation coefficient. The peak of the distribution is located at $\psi = \theta$. Fig. 1 shows distributions for $n = 1, 2, 4$, and 8, $|\rho_c| = 0.7$, and $\theta = 0$. It is evident that multilook processing improves the phase accuracy. It can be shown that when $|\rho_c| = 0$, the PDF is uniformly distributed, and that when $|\rho_c| = 1$, the PDF becomes a Derac delta function. A plot of standard deviation versus $|\rho_c|$ is given in Fig. 2, which verifies a similar but less accurate figure (see Zebker [4]) computed with interferometric radar data. As shown in Fig. 2, multilook processing effectively reduces the phase error, especially when $n = 16$ and 32.

V. Distribution of the Multilook $|S_i S_j^*|$

The magnitude of product of S_i and S_j is an important measure in polarimetric SAR, and represents the magnitude of the interferogram. The normalized magnitude is defined as

$$\xi = \frac{\left|\frac{1}{n}\sum_{k=1}^{n} S_i(k)S_j^*(k)\right|}{\sqrt{E[|S_i|^2]E[|S_j|^2]}} = \frac{g}{h} \quad (25)$$

where g is the multilook $|S_i S_j^*|$. The PDF of ξ (Lee *et al.* [7]) derived by integrating (17) with respect to B_1, B_2, and ψ, is

$$p(\xi) = \frac{4n^{n+1}\xi^n}{\Gamma(n)(1 - |\rho_c|^2)} I_0\left(\frac{2|\rho_c|n\xi}{1 - |\rho_c|^2}\right) \cdot K_{n-1}\left(\frac{2n\xi}{1 - |\rho_c|^2}\right) \quad (26)$$

where $I_0(\,)$ and $K_n(\,)$ are modified Bessel functions. The PDF for the unnormalized magnitude g is obtained from (26) using (25):

$$p(g) = \frac{4n^{n+1}g^n}{\Gamma(n)(1 - |\rho_c|^2)h^{n+1}} I_0\left(\frac{2|\rho_c|ng/h}{1 - |\rho_c|^2}\right) \cdot K_{n-1}\left(\frac{2ng/h}{1 - |\rho_c|^2}\right). \quad (27)$$

In this section, we shall confine our discussion to the statistics of ξ. The standard deviations of ξ is plotted versus the correlation coefficient in Fig. 3. As expected, the multilook processing reduces the standard deviation. However, contrary to the characteristics of the phase-difference PDF, the standard deviation of this product increases as the correlation coefficient increases. This property can be explained by the Schwartz inequality [8].

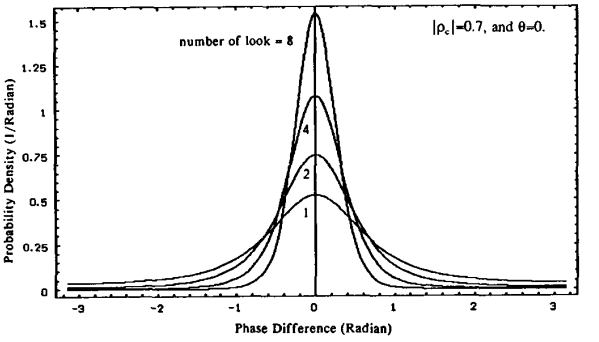

Fig. 1. Plots of phase difference distribution for the number of looks $n = 1, 2, 4$, and 8, with the magnitude of complex correlation coefficient $|\rho_c| = 0.7$ and its phase $\theta = 0$. Note that the phase difference variation is reduced as the number of looks increases.

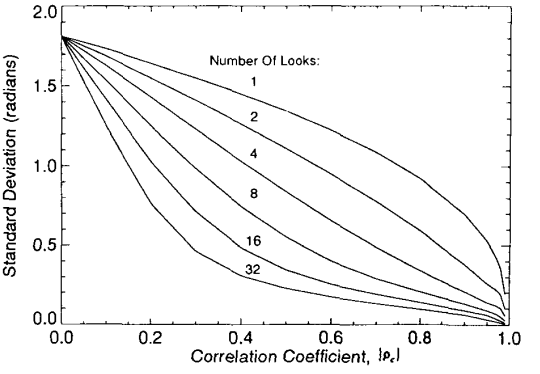

Fig. 2. Phase difference standard deviations versus the correlation coefficient $|\rho_c|$ for the number of looks $n = 1, 2, 4, 8, 16$, and 32. The phase of the complex correlation coefficient $\theta = 0$.

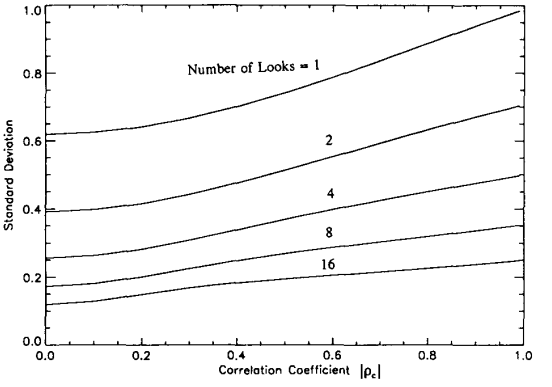

Fig. 3. Standard deviations of normalized magnitude of product (i.e., interogram) versus correlation coefficient $|\rho_c|$ for the number of looks $n = 1, 2, 4, 8$, and 16.

VI. Joint Distribution of Multilook $|S_i|^2$ and $|S_j|^2$

The PDF of joint returns from two correlated channels of polarimetric and interferometric radars is of impor-

tance, especially, when only incomplete polarimetric data are available. Data from the JPL AIRSAR synoptic processor [7], from NADC/ERIM SAR, and from SIR-B with different look angles are examples. In addition, this joint PDF will lead to the derivation of the intensity and amplitude ratio PDF's. From (16), we let the multilook intensities be

$$R_1 = \frac{1}{n}\sum_{k=1}^{n}|S_i(k)|^2 = \frac{B_1 C_{11}}{n}$$
$$R_2 = \frac{1}{n}\sum_{k=1}^{n}|S_j(k)|^2 = \frac{B_2 C_{22}}{n} \tag{28}$$

where again, $C_{ii} = E[|S_i|^2]$. For convenience, the joint PDF of B_1 and B_2 is derived first. It is obtained by integrating (17) with respect to η and ψ. The derivation is given in Appendix B. The PDF is

$$p(B_1, B_2) = \frac{(B_1, B_2)^{(n-1)/2}\exp\left(-\dfrac{B_1 + B_2}{1 - |\rho_c|^2}\right)}{\Gamma(n)(1 - |\rho_c|^2)|\rho_c|^{n-1}} \cdot I_{n-1}\left(2\sqrt{B_1 B_2}\,\frac{|\rho_c|}{1 - |\rho_c|^2}\right). \tag{29}$$

Using (28), we have the joint distribution of R_1 and R_2

$$p(R_1, R_2) = \frac{n^{n+1}(R_1 R_2)^{(n-1)/2}\exp\left[-\dfrac{n(R_1/C_{11} + R_2/C_{22})}{1 - |\rho_c|^2}\right]}{(C_{11}C_{22})^{(n+1)/2}\Gamma(n)(1 - |\rho_c|^2)|\rho_c|^{n-1}} I_{n-1}\left(2n\sqrt{\frac{R_1 R_2}{(C_{11}C_{22})}}\,\frac{|\rho_c|}{1 - |\rho_c|^2}\right). \tag{30}$$

To facilitate feature classifications with two intensity SAR images, a distance measure can be derived from (30) using the same procedure of Kong [1].

VII. Multilook Intensity and Amplitude Ratio Distributions

The intensity and amplitude ratios between S_{hh} and S_{vv} have been important discriminators in the study of polarimetric radar returns. The 1-look amplitude PDF has been shown by Kong [1]. In this section, PDF's of normalized ratios of intensity and amplitude will be presented. The derivation is shown in Appendix C. Let the normalized intensity ratio be

$$\mu = \frac{B_1}{B_2} = \frac{\sum_{k=1}^{n}|S_i(k)|^2/C_{11}}{\sum_{k=1}^{n}|S_j(k)|^2/C_{22}} = \frac{\sum_{k=1}^{n}|S_i(k)|^2}{\tau\sum_{k=1}^{n}|S_j(k)|^2}. \tag{31}$$

where $\tau = C_{11}/C_{22}$. The PDF for the multilook normalized intensity ratio is

$$p^{(n)}(\mu) = \frac{\Gamma(2n)(1 - |\rho_c|^2)^n(1 + \mu)\mu^{n-1}}{\Gamma(n)\Gamma(n)[(1 + \mu)^2 - 4|\rho_c|^2\mu]^{(2n+1)/2}}. \tag{32}$$

Let $v = \sqrt{\mu}$. The multilook normalized amplitude ratio can be easily derived from (32);

$$p^{(n)}(v) = \frac{2\Gamma(2n)(1 - |\rho_c|^2)^n(1 + v^2)v^{2n-1}}{\Gamma(n)\Gamma(n)[(1 + v^2)^2 - 4|\rho_c|^2v^2]^{(2n+1)/2}}. \tag{33}$$

The PDF's of the intensity and amplitude ratios between the multilook S_1 and S_2 are easily derived from (32) and (33). From (31), let

$$w = \frac{\sum_{k=1}^{n}|S_1(k)|^2}{\sum_{k=1}^{n}|S_2(k)|^2} = \tau\mu \qquad z = \sqrt{w} = \sqrt{\tau}\,v. \tag{34}$$

The PDF of the multilook intensity ratio w is

$$p^{(n)}(w) = \frac{\tau^n\Gamma(2n)(1 - |\rho_c|^2)^n(\tau + w)w^{n-1}}{\Gamma(n)\Gamma(n)[(\tau + w)^2 - 4\tau|\rho_c|^2w]^{(2n+1)/2}}. \tag{35}$$

The PDF of the multilook amplitude ratio z is

$$p^{(n)}(z) = \frac{2\tau^n\Gamma(2n)(1 - |\rho_c|^2)^n(\tau + z^2)z^{2n-1}}{\Gamma(n)\Gamma(n)[(\tau + z^2)^2 - 4\tau|\rho_c|^2z^2]^{(2n+1)/2}}. \tag{36}$$

For $n = 1$, (36) reduces to the 1-look amplitude ratio distribution, which is identical to the results of Kong [1].

We shall limit the discussion to the statistics of the normalized amplitude ratio v. Fig. 4 shows plots of PDF's at various number of looks for $|\rho_c| = 0.5$. It clearly shows that the distribution becomes narrower, and concentrated ner 1.0. In other words, multilook processing reduces the statistical variation. The standard deviation of v is plotted versus the correlation coefficient in Fig. 5, for $n = 1$, 2, 4, 8, and 16. It shows that the strandard deviation decreases as the correlation or the number of looks increases.

VIII. Comparison of Theoretical PDF's with Measurements

In this section, to verify this complex Gaussian model, the NASA/JPL AIRSAR polarimetric data of San Francisco, California, and Howland Forest, Maine (Fig. 6) were used to compare histograms and their corresponding PDF's of phase differences, normalized products, and amplitude ratios. Homogeneous regions of forest, ocean, park areas, and city blocks were selected to compute the complex correlation coefficient (i.e., θ and $|\rho_c|$) and histograms. We have checked the 1-look C-band and L-band data of Howland Forest, and found that the agreements between histograms and their corresponding PDF's are good except the magnitude of product (see Fig. 7). The

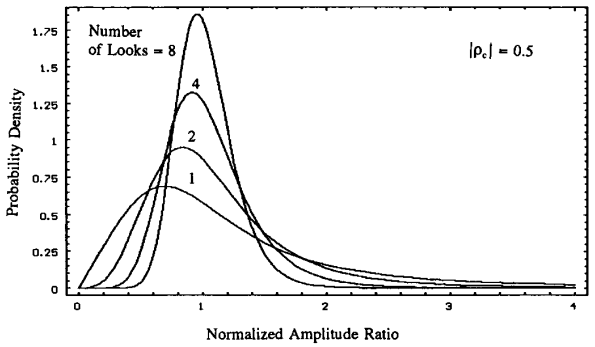

Fig. 4. Normalized amplitude ratio distributions for the number of looks $n = 1, 2, 4$, and 8 with $|\rho_c| = 0.5$. The distributions become sharper and centered near 1.0 as the number of looks increases.

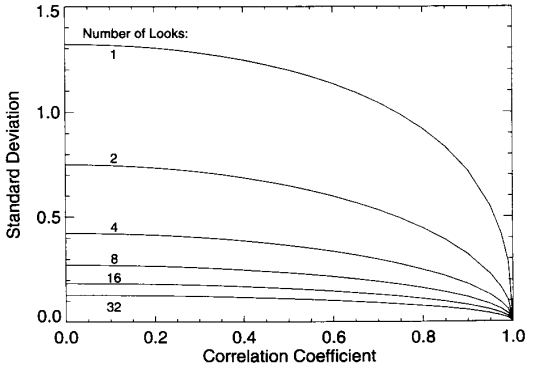

Fig. 5. Plots of standard deviations versus correlation coefficients for the number of looks $n = 1, 2, 4, 8, 16$, and 32. It indicates that the standard deviation of the distributions is reduced as either the number of looks or the correlation coefficient increases.

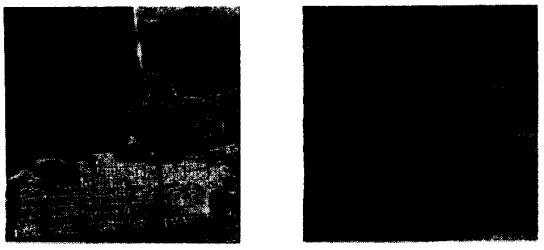

(a) (b)

Fig. 6. JPL/AIRSAR 4-look images (512 × 512 pixels). (a) San Francisco scene and (b) Howland Forest scene.

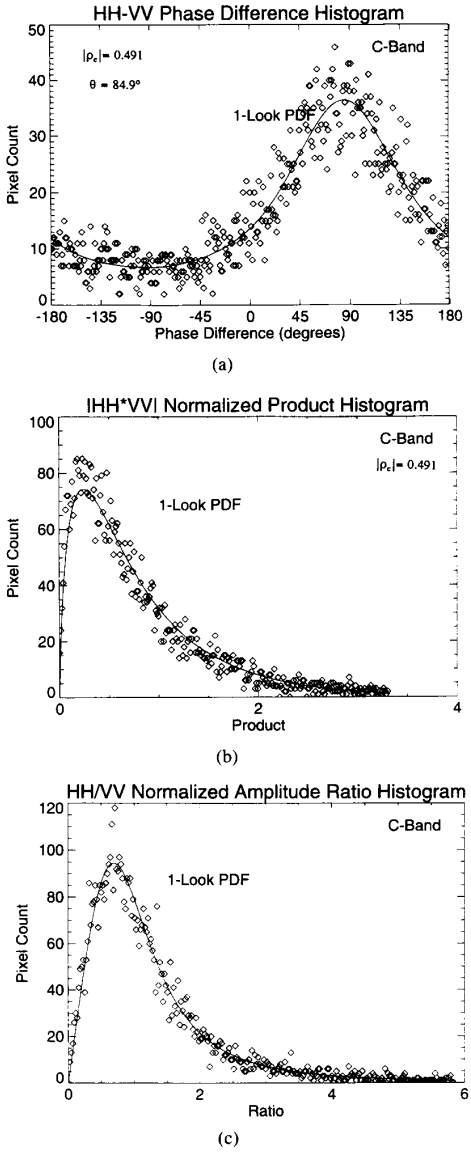

Fig. 7. Experimental results using 1-look AIRSAR data of Howland Forest (HR1804C) with $|\rho_c| = 0.491$ and $\theta = 84.9°$. (a) The histogram of phase difference between *HH* and *VV* and the theoretical 1-look PDF. The agreement is good. (b) The histogram and the 1-look PDF of the normalized product of *HH* and *VV*. (c) The histogram and the 1-look PDF of the normalized *HH/VV*. The match is good. Histograms are shown in ◇.

reason for the somewhat mismatch of the product magnitude is due to the inadequate modelling with a Gaussian distribution [13]. A detailed discussion on this issue will be given in Section IX.

Using 4-look Howland Forest data (CM1084), we found that discrepancies exist for all three distributions. The match between histograms and 4-look phase-difference PDF's are not as good as those of the 1-look data (see Fig. 8). A better match was found with 3-look PDF's (see Fig. 9). The problem was traced to the averaging of correlated neighboring pixels during the multilook processing, because the 1-look AIRSAR data are oversampled to preserve the spatial resolution. To verify this, the spatial correlations between immediate neighboring pixels and between every other pixel in the azimuthal direction were computed using all three components (*HH*, *VV*, and *HV*) of (2). Table I shows that the magnitudes of the correlation between neighboring pixels is consistently much higher than that between every other pixels. For illustration, we used 1-look data of Howland Forest (HR1084C) and performed the 4-look processing by averaging 4 pixels separated by 2 pixels in the azimuth direction. Since the correlation between every other pixels

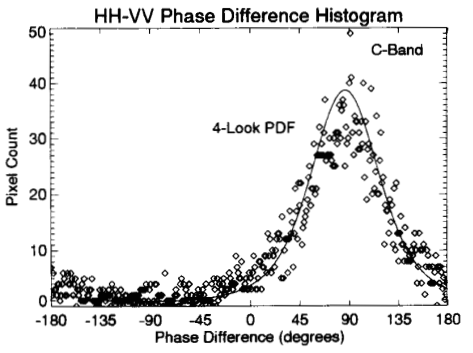

(a)

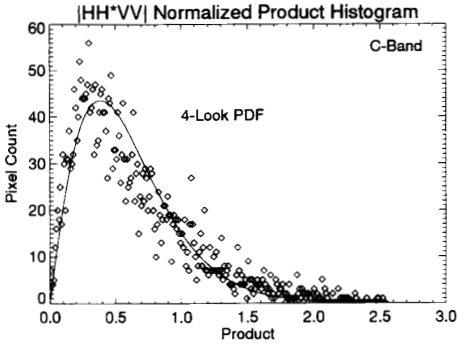

(b)

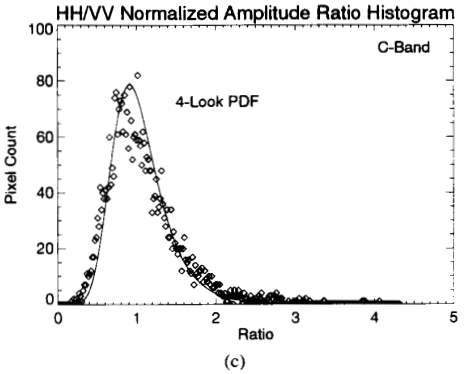

(c)

Fig. 8. Experimental results using 4-look AIRSAR data of Howland Forest (CM1804C) with $|\rho_c| = 0.491$ and $\theta = 84.9°$. (a) The histogram of the phase difference between *HH* and *VV* and the theoretical 4-look PDF. (b) The histogram and the 4-look PDF of the normalized product of *HH* and *VV*. (c) The histogram and the 4-look PDF of the normalized *HH/VV*. Discrepancies were found in the agreement between histograms and their corresponding PDF's. The problem is traced to the averaging of correlated 1-look pixels during the multilook processing.

is much less than that between its immediate neighbors, statistical independence is assured. The results are shown in Fig. 10 for all three distributions under study. The agreement with 4-look PDF's is good. We can conclude that due to the correlation of 1-look data, the 4-look AIRSAR data have characteristics close to the 3-look data. Other studies [9], using the speckle index of multilook intensity and/or amplitude, have also reached the same conclusion.

We also compared the results of ocean, park areas, and

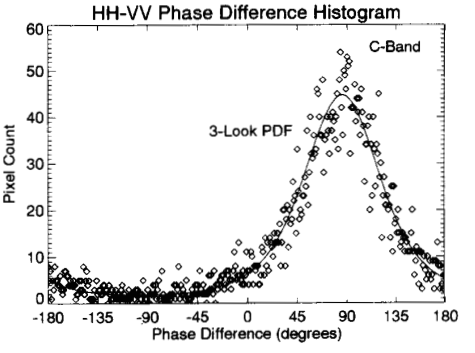

(a)

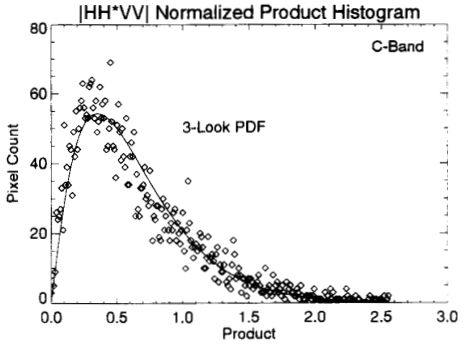

(b)

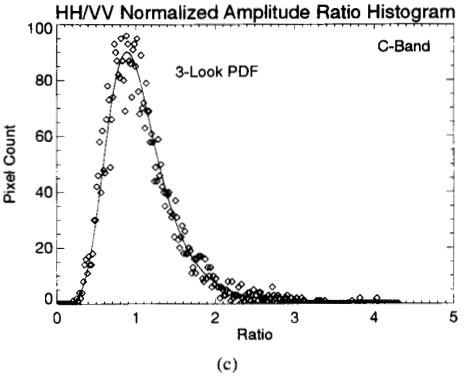

(c)

Fig. 9. The same histograms of Fig. 8 are plotted with their corresponding theoretical 3-look PDF's. The agreement is much better. (a) the histogram and the 3-look PDF of the phase difference. (b) The histogram and the 3-look PDF of normalized magnitude of product. (c) The histogram and the 3-look PDF of normalized *HH/VV*.

TABLE I
SPATIAL CORRELATION BETWEEN IMMEDIATE NEIGHBORING PIXELS OF JPL 1-LOOK POLARIMETRIC SAR IS MUCH HIGHER THAN THAT BETWEEN EVERY OTHER PIXEL. THIS EXPLAINS WHY JPL 4-LOOK PROCESSED AIRSAR IMAGERY HAS THE CHARACTERISTICS OF A 3-LOOK PROCESSED IMAGERY (C-BAND HOWLAND FOREST 1-LOOK DATA IS USED)

Spatial Correlation		$\lvert\rho_c\rvert$	Phase (degree)
Between nearest neighbors	HH	0.524	137.2
	HV	0.513	137.2
	VV	0.513	133.2
Between every other neighbors	HH	0.0592	118.5
	HV	0.0473	68.8
	VV	0.0462	75.0

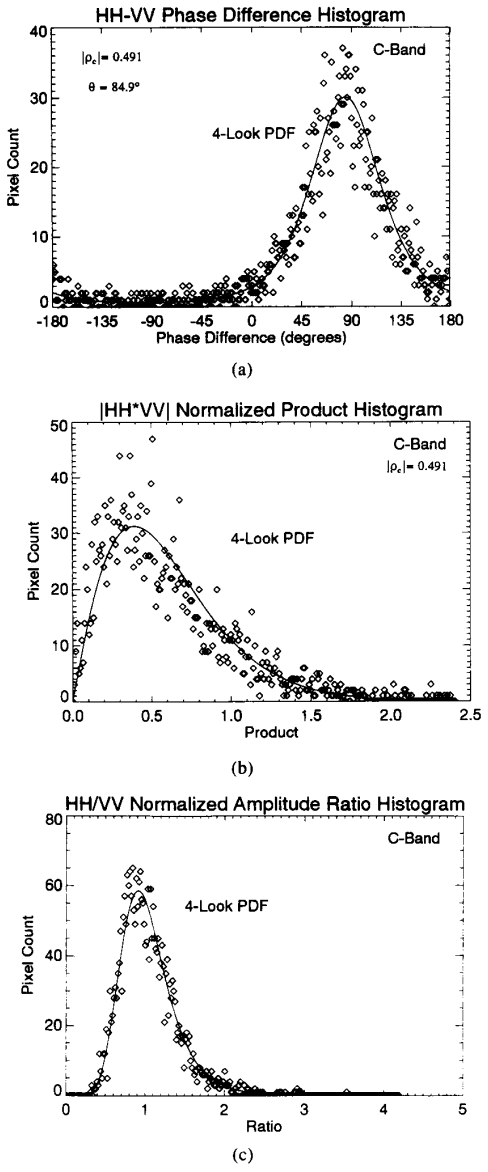

Fig. 10. Using 1-look AIRSAR Howland Forest data (HR1084C), the 4-look data were computed by averaging pixels separated by a distance of two pixels to reduce correlations between pixels in the multilook processing. The agreement between histograms and their corresponding PDF's are good. The results of Fig. 9 and Fig. 10 substantiate that the 4-look AIRSAR data has the characteristics of a 3-look. (a) *HH/VV* phase-difference histogram and the 4-look PDF. (b) The histogram of normalized $|HH^*VV|$ and the 4-look PDF. (c) The histogram of normalized $|HH|/|VV|$ and the 4-look PDF.

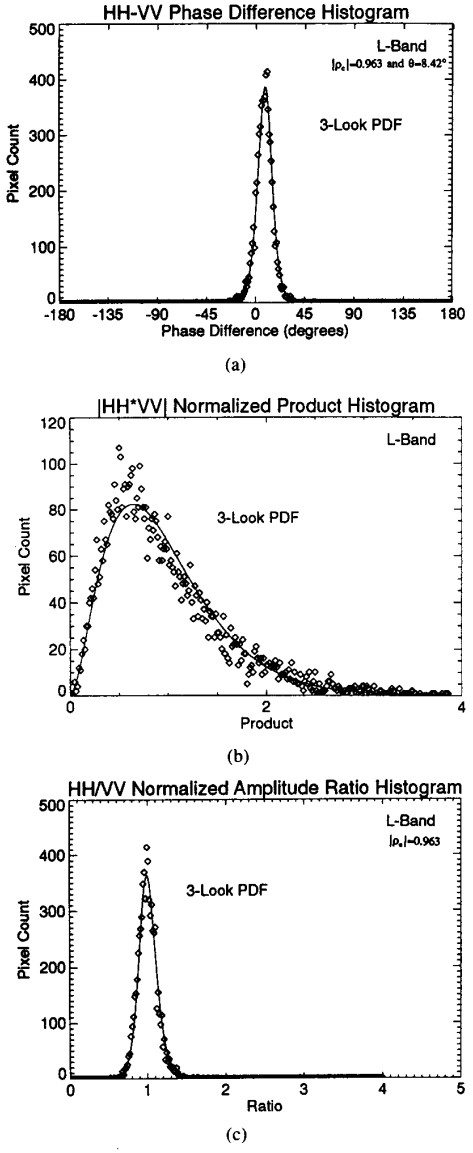

Fig. 11. Experimental results of an ocean area, using 4-look AIRSAR data from San Francisco. The good agreement between all three distributions are clearly shown. (a) Phase difference. (b) Normalized product. (c) Normalized amplitude ratio.

city blocks from 4-look San Francisco scene. The agreement in the ocean areas ($|\rho_c| = 0.963$) is very good in all three distributions (see Fig. 11). It also shows that the higher correlation between the *HH* and *VV* components sharpens the distributions of the phase difference and the ratio, but not the normalized product. In the park and city areas, the inhomogeneity makes the Gaussian assumption invalid. However, experimentally, we found that the agreement is good in the phase difference and the ratio distributions (see Fig. 12), but the normalized product shows strong disagreement with the theoretical PDF's (histograms not shown). The correlation coefficients for the park and city areas are lower with 0.274 and 0.342, respectively.

IX. Remarks and Discussions

1) The number of looks n in the PDF's of this paper was assumed to be an integer. Mathematically, this assumption was not needed in the derivations. Consequently, for the precision of matching histograms with PDF's, the number of looks can take a fractional value.

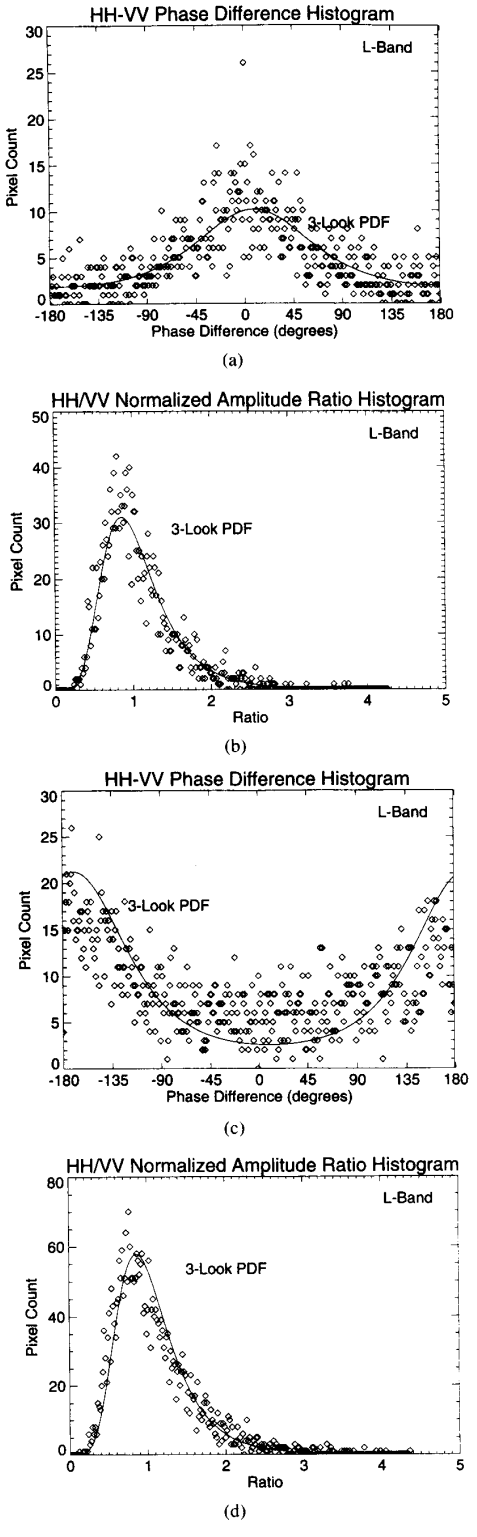

Fig. 12. Experimental results of park and city areas, using 4-look AIR-SAR data from San Francisco. The agreement between histograms and their corresponding 3-look PDF's are reasonably good for the *HH/VV* phase difference and normalized *HH/VV*. (a) and (b) are for the park area, and (c) and (d) are for the city block area.

2) Many nonpolarimetric studies have shown that terrain radar clutter may not be adequately modeled with a Gaussian distribution due to the texture variation. The K-distribution [13] has proved to be useful in characterizing the amplitude distribution for some ground covers. For 1-look polarimetric SAR imagery, the K-distribution was derived in [14] by the product of a Gamma-distributed random variable and the Gaussian distributed complex random vector of (2). The phase difference and the amplitude and intensity ratio distributions, consequently, are independent of the Gamma distribution [13]. For multilook polarimetric processing, the agreement of histograms and theoretical PDF's of this paper strongly support this conclusion. Discrepancies observed in the distributions of the magnitude of complex product, for forest, city, and park areas, indicate the need of a better multilook model similar to the 1-look K-distribution.

3) For interferometric radar, the decorrelation effects [4] due to the baseline, thermal noise, temporal variation, and so on, cause the broadening of the phase-difference distribution. Multilook processing [12] is effective in reducing statistical variations by averaging spatially in the complex interferogram. The multilook phase PDF derived in this paper can be used for the error estimation.

X. Conclusion

The statistics of multilook polarimetric and interferometric radar data have been investigated. The PDF's of the multilook phase difference, the magnitude of product, and the intensity and amplitude ratios were derived, and expressed in closed form. Experimental results using multilook polarimetric SAR data indicated good agreement for phase difference and amplitude ratio for various ground covers. The magnitude of product, however, showed good agreement in the ocean areas, but an inadequacy of the Gaussian model to match the data was found in forest areas. Explanations using K-distribution have been provided. The statistics derived in this paper should prove useful in the study of polarimetry and interferometry.

Appendix A

This appendix is devoted to prove (11), which establishes the relation between the complex correlation coefficient and the multilook intensity correlation coefficient. Let the two scattering matrix components (i.e., 1-look)

$$S_i = a_R + ia_I$$
$$S_j = b_R + ib_I \tag{A1}$$

where S_i and S_j are jointly circular Gaussian distributed. The complex correlation coefficient or (9) is converted into

$$\rho_c = \frac{E[(a_R + ia_I)(b_R - ib_I)]}{\sqrt{E[a_R^2 + a_I^2]E[b_R^2 + b_I^2]}}. \tag{A2}$$

For convenience, let correlation coefficients between real and imaginary parts of S_i and S_j

$$\rho_{RR} = \frac{E[a_R b_R]}{\sigma_a \sigma_b} \qquad \rho_{RI} = \frac{E[a_R b_I]}{\sigma_a \sigma_b}$$

$$\rho_{IR} = \frac{E[a_I b_R]}{\sigma_a \sigma_b} \qquad \rho_{II} = \frac{E[a_I b_I]}{\sigma_a \sigma_b} \tag{A3}$$

where σ_a is the standard deviation of a_R and a_I. The σ_b is similarly defined.

Substituting the above equations into (A2) yields

$$\rho_c = \frac{(\rho_{RR} + \rho_{II}) + i(\rho_{IR} - \rho_{RI})}{2}. \tag{A4}$$

The circular Gaussian condition demands

$$\rho_{RR} = \rho_{II} \qquad \rho_{IR} = -\rho_{RI}. \tag{A5}$$

Applying the above relations, we have

$$|\rho_c|^2 = \rho_{RR}^2 + \rho_{IR}^2. \tag{A6}$$

The multilook processing produces

$$A_n = \frac{1}{n} \sum_{k=1}^{n} [a_R(k)^2 + a_I(k)^2]$$

$$B_n = \frac{1}{n} \sum_{k=1}^{n} [b_R(k)^2 + b_I(k)^2]. \tag{A7}$$

Using the assumption of statistical independence between samples, the means and standard deviations (SD) of (A7) are

$$\bar{A}_n = E[A_n] = 2E[a_R(k)^2] = 2\sigma_a^2 \qquad \text{SD}[A_n] = \frac{2\sigma_a^2}{\sqrt{n}}$$

$$\bar{B}_n = E[B_n] = 2E[b_R(k)^2] = 2\sigma_b^2 \qquad \text{SD}[B_n] = \frac{2\sigma_b^2}{\sqrt{n}}. \tag{A8}$$

The multilook correlation coefficient for intensity (see (10)) can be written as

$$\rho_I^{(n)} = \frac{E[(A_n - \bar{A}_n)(B_n - \bar{B}_n)]}{\text{SD}[A_n]\,\text{SD}[B_n]}. \tag{A9}$$

Again using the assumption of statistical independence between samples, after manipulations, the numerator of (A9) becomes

$$E[(A_n - \bar{A}_n)(B_n - \bar{B}_n)] = \frac{1}{n^2} \sum_{k=1}^{n} [E[(a_R(k)^2 + a_I(k)^2)(b_R(k)^2 + b_I(k)^2)] - 4\sigma_a^2\sigma_b^2]]. \tag{A10}$$

From Papoulis [10, p. 221], the following identity has been established for two Gaussian distributed random variables, x and y:

$$E[x^2y^2] = \sigma_x^2\sigma_y^2(1 + \rho_{xy}^2). \tag{A11}$$

Utilizing the above equation and (A3), (A5), and (A6), the numerator is simplified to

$$E[(A_n - \bar{A}_n)(B_n - \bar{B}_n)] = \frac{4}{n}\sigma_a^2\sigma_b^2|\rho_c|^2.$$

By substituting the above equation into (A9), the proof of (11) is complete.

Appendix B

In this appendix, we derive the joint PDF of B_1 and B_2. Integrating $p(B_1, B_2, \eta, \psi)$ of (17) with respect to ψ, yields

$$p(B_1, B_2, \eta) = \frac{2\eta(B_1B_2 - \eta^2)^{n-2}}{\Gamma(n)\Gamma(n-1)(1-|\rho_c|^2)^n} \cdot \exp\left(-\frac{B_1 + B_2}{1-|\rho_c|^2}\right) I_0\left(\frac{2\eta|\rho_c|}{1-|\rho_c|^2}\right). \tag{B1}$$

Let

$$\chi = \frac{\eta}{\sqrt{B_1B_2}}.$$

Integrating with respect to η, (B1) then yields

$$p(B_1, B_2) = \frac{2(B_1B_2)^{n-1}\exp\left(-\frac{B_1+B_2}{1-|\rho_c|^2}\right)}{\Gamma(n)\Gamma(n-1)(1-|\rho_c|^2)^n} \cdot \int_0^1 (1-\chi^2)^{n-2}\chi I_0\left(\frac{2|\rho_c|}{1-|\rho_c|^2}\sqrt{B_1B_2}\chi\right)d\chi. \tag{B2}$$

Applying integration identity from Prudnikov *et al.* [15, p. 302, eq. 5], we have

$$p(B_1, B_2) = \frac{(B_1B_2)^{n-1}\exp\left(-\frac{B_1+B_2}{1-|\rho_c|^2}\right)}{\Gamma(n)\Gamma(n)(1-|\rho_c|^2)^n} \cdot {}_1F_2\left[\begin{matrix}1;\\ 1, n;\end{matrix} \quad B_1B_2\left(\frac{|\rho_c|}{1-|\rho_c|^2}\right)^2\right]. \tag{B3}$$

Applying the following identity:

$$I_\mu(z) = \frac{(z/2)^\mu}{\Gamma(\mu+1)}\,{}_0F_1[-;\ \mu+1;\ z^2/4]$$

we have

$$p(B_1, B_2) = \frac{(B_1B_2)^{(n-1)/2}\exp\left(-\frac{B_1+B_2}{1-|\rho_c|^2}\right)}{\Gamma(n)(1-|\rho_c|^2)|\rho_c|^{n-1}} \cdot I_{n-1}\left(2\sqrt{B_1B_2}\frac{|\rho_c|}{1-|\rho_c|^2}\right). \tag{B4}$$

Appendix C

The PDF of the multilook normalized intensity ratio equation (32) can be derived by applying the following

integration (Papoulis [10, p. 197, eq. (7-21)]:

$$p(\mu) = \int_0^\infty B_2 p(\mu B_2, B_2)\, dB_2 \qquad \text{(C1)}$$

where $p(\mu B_2, B_2)$ is the joint PDF of B_1 and B_2 of (B4). Substituting (B4) into (C1), we have

$$p(\mu) = \frac{\mu^{(n-1)/2}}{\Gamma(n)(1 - |\rho_c|^2)|\rho_c|^{n-1}} \int_0^\infty B_2^n \cdot \exp\left(-\frac{B_2(1+\mu)}{1-|\rho_c|^2}\right) \cdot I_{n-1}\left(2B_2\sqrt{\mu}\,\frac{|\rho_c|}{1-|\rho_c|^2}\right) dB_2. \qquad \text{(C2)}$$

Using an integration identity from Prudnikov *et al.* [15, p. 303, eq. 2], the integral of (C2) becomes

$$\left(\frac{1+\mu}{1-|\rho_c|^2}\right)^{-2n} \left(\frac{\sqrt{\mu}\,|\rho_c|}{1-|\rho_c|^2}\right)^{n-1} \frac{\Gamma(2n)}{\Gamma(n)} \cdot {}_2F_1\left(n, (2n+1)/2; n; \frac{4|\rho_c|^2\mu}{(1+\mu)^2}\right). \qquad \text{(C3)}$$

The hypergeometric function can be simplified into

$${}_1F_0\left((2n+1)/2; -; \frac{4\mu|\rho_c|^2}{(1+\mu)^2}\right) = [(1+\mu)^2 - 4\mu|\rho_c|^2]^{(2n+1)/2}(1+\mu)^{2n+1}. \qquad \text{(C4)}$$

Using (C3) and (C4), after manipulations, (C2) yields

$$p^{(n)}(\mu) = \frac{\Gamma(2n)(1-|\rho_c|^2)^n(1+\mu)\mu^{n-1}}{\Gamma(n)\Gamma(n)[(1+\mu)^2 - 4|\rho_c|^2\mu]^{n+1/2}}. \qquad \text{(C5)}$$

REFERENCES

[1] J. A. Kong *et al.*, "Identification of terrain cover using the optimal polarimetric classifier," *J. Electromagnet. Waves Applicat.*, vol. 2, no. 2, pp. 171-194, 1987.

[2] K. Sarabandi, "Derivations of phase statistics from the Mueller matrix," *Radio Sci.*, vol. 27, no. 5, pp. 553-560, 1992.

[3] N. R. Goodman, "Statistical analysis based on a certain complex Gaussian distribution (an introduction)," *Ann. Mathemat. Statist.*, vol. 34, pp. 152-177, 1963.

[4] H. A. Zebker and J. Villasenor, "Decorrelation in interferometric radar echoes," *IEEE Trans. Geosci. Remote Sensing*, vol. 30, pp. 950-959, Sept. 1992.

[5] J. W. Goodman, *Statistical Optics*. New York: Wiley, 1985.

[6] V. B. Tayloer, "CYLOPS: The JPL AITSAR synoptic processor," in *Proc. 1992 Int. Geosci. Remote Sensing Symp.* (IGARSS'92), Houston, TX, 1992, pp. 652-654.

[7] J. S. Lee, A. R. Miller, and K. Hoppel, "Statistics of phase difference and product magnitude of multilook processed Gaussian signals," *Waves in Random Media*. IOP Publishing Inc., London, UK (to appear).

[8] H. Stark and J. W. Woods, *Probability, Random Processes, and Estimation Theory for Engineers*. Englewood Cliffs, NJ: Prentice-Hall, 1986.

[9] J. S. Lee and K. Hoppel, "Principal components transformation of multifrequency polarimetric SAR imagery," *IEEE Trans. Geosci. Remote Sensing*, vol. 30, pp. 686-696, July 1992.

[10] A. Papoulis, *Probability, Random Variables, and Stochastic Processes*. New York: McGraw-Hill, 1965.

[11] J. J. van Zyl, H. A. Zebker, and C. Elachi, "Imaging radar polarimetric signatures: Theory and observation," *Radio Sci.*, vol. 22, pp. 529-543, 1987.

[12] F. Li and R. M. Goldstein, "Studies of multi-baseline spaceborne interferometric synthetic aperture radars," *IEEE Trans. Geosci. Remote Sensing*, vol. 28, pp. 88-97, Jan. 1990.

[13] S. H. Yueh, J. A. Kong, J. K. Jao, R. T. Shin, and L. M. Novak, "*K*-distribution and polarimetric terrain radar clutter," *J. Electromagnet. Waves Applicat.*, vol. 3, no. 8, pp. 747-768, 1989.

[14] L. M. Novak, M. B. Sechtin, and M. J. Cardullo, "Studies on target detection algorithms which use polarimetric radar data," *IEEE Trans. Aerospace Electron. Syst.*, vol. 25, March 1989.

[15] A. P. Prudnikov, Y. A. Brychkov, and I. O. Maichev, *Integrals and Series*, vol. 2. New York: Gordon and Breach, 1986.

[16] L. P. Murza, "The noncoherent polarimetry of noiselike radiation," *Radio Eng. Electron. Phys.*, pp. 57-63, July 1978.

[17] A. Lopes *et al.*, "Phase difference statistics related to sensor and forest parameters," in *Proc. Int. Geosci. Remote Sensing Symp.* (IGARSS'92) Houston, TX, 1992, pp. 779-781.

[18] H. H. Lim *et al.*, "Classification of earth terrain using polarimetric synthetic aperture radar images," *J. Geophys. Res.*, vol. 94, no. B6, pp. 7049-7057, 1989.

[19] J. S. Lee and M. R. Grunes, "Feature classification using multi-look polarimetric SAR imagery," in *Proc. Int. Geosci. Remote Sensing Symp.* (IGARSS'93), Houston, TX, 1992, pp. 77-79.

Jong-Sen Lee (S'66-M'69-SM'91) received the B.S. degree in electrical engineering from the National Cheng-Kung University, Taiwan, in 1963, and the A.M. and Ph.D. degrees from Harvard University, Cambridge, MA, in 1965 and 1969, respectively.

Since then he has been with the U.S. Naval Research Laboratory (NRL), Washington DC, where he is presently the Head of the Image Science Section, Remote Sensing Division. He is also the principal investigator of the remote sensing program on frequency and polarization diversities. He developed several speckle filtering algorithms for SAR images, which have been implemented in many GIS software packages. His research covers a wide spectrum of areas. He worked on control theory, operations research, radiative transfer, image processing, and SAR processing, image segmentation, speckle analysis, and filtering. His current research interests are in the area of multifrequency SAR image segmentation, statistical analysis, scattering signature modeling, and SAR interferometry.

Karl W. Hoppel received the B.Sc. degree in physics from the University of Maryland, College Park, in 1987 and the M.Sc. degree in applied physics from George Mason University, Fairfax, VA, in 1992.

He is currently working on his doctorate in computational physics. From 1985 to 1986 he worked part time on contract to General Electric and designed computer models of the electrical environment near dc power lines. From 1987 to 1993 he was with Allied Signal Technical Services in support of the Naval Research Laboratory. He worked on SAR processing, image processing, data compression, and air-sea interaction experiments. Since 1993 he has been a research physicist with the Remote Sensing Division, Naval Research Laboratory. He is currently working on SAR and LIDAR applications in remote sensing.

Stephen A. Mango received the B.S. degree in physics and mathematics from Fairfield University, Fairfield, CT, in 1964 and the Ph.D. degree in astronomy/astrophysics from Georgetown University, Washington, DC, in 1971.

He was an NRC/NAS Postdoctoral Fellow in radio astronomy with the Space Sciences Divison, Naval Research Laboratory. Since then he has been with the Naval Research Laboratory, where is he presently the Head of the Imaging Systems and Research Branch and the Digital Image Processing Laboratory, Remote Sensing Divison. His research areas have included spectroscopy of planetary atmospheres, solar ultraviolet physics, atmospheric propagation, radio astronomical research on interstellar molecules, and very-long-baseline interferometry, imaging systems, and image coding. Since 1974 he has concentrated on remote sensing research and applications utilizing imaging radar technologies, with a special emphasis on signal and image processing of synthetic aperture radar.

Allen R. Miller was born in Brooklyn, NY, on December 2, 1942. He studied mathematics at Brooklyn College, the University of Maryland at College Park, and the Polytechnic Institute of Brooklyn.

Between 1965 and 1967 he served two years in the Ordnance Corps, U.S. Army. From 1968 to 1993 he worked as a mathematician with the Naval Research Laboratory. Just before retiring from the NRL, he joined the faculty of George Washington University, Washington, DC, as a research professor of mathematics. He has written or coauthored nearly 40 papers on pure and applied mathematics.